Geologically-rapid aqueous mineral alteration at subfreezing temperatures in icy worlds

Amber Zandanel, Roland Hellmann, Laurent Truche, Vladimir Roddatis, Michel Mermoux, Gaël Choblet, Gabriel Tobie

Geologically-rapid aqueous mineral alteration at subfreezing temperatures in icy worlds

Amber Zandanel[1*], Roland Hellmann[1], Laurent Truche[1], Vladimir Roddatis[2], Michel Mermoux[3], Gaël Choblet[4], Gabriel Tobie[4]

[1] Université Grenoble Alpes, CNRS, ISTerre, F-38058 Grenoble Cedex 9, France

[2] GFZ German Research Centre for Geosciences, Telegrafenberg, D-14473 Potsdam, Germany

[3] Université Grenoble Alpes, Univ. Savoie Mont Blanc, CNRS, Grenoble INP, LEPMI, 38000 Grenoble, France

[4] Laboratoire de Planétologie et Géodynamique, UMR 6112, CNRS, Université de Nantes, 2 chemin de la Houssinière, 44300 Nantes, France

*azandanel@gmail.com

The most active icy worlds like Europa or Enceladus are predicted to host extensive aqueous alteration driven by water-rock interactions at elevated temperatures[1–3]. On the other hand, it is assumed that such alteration is kinetically inhibited at the sub-zero temperatures of other icy worlds, such as the mid-sized moons of Saturn and Uranus or Trans-Neptunian Objects[1,4]. Here we perform aqueous alterations experiments on a chondrite-analogue material (olivine) and find that chemical alteration processes are still efficient at temperatures as low as -20 °C, as the presence of an unfrozen water film still allows olivine to dissolve in partially frozen alkaline solutions. We infer that aqueous alteration may be enhanced by salts and ammonia present in icy worlds, and therefore remains a geologically rapid process even at sub-zero temperatures. Our results imply that most icy bodies exceeding 400-500 km in diameter will be completely altered to hydrous secondary minerals early in their evolutionary histories.

Models of icy worlds evolution often anticipate the release of heat and chemical energy through aqueous alteration or serpentinization of primary chondritic minerals when in contact with fully melted water[4–6]. One fundamental question is whether bulk liquid water is a necessary prerequisite to these processes, or can water-rock interactions still occur below the freezing point in icy bodies? To address this, we determined the rates and mechanism of olivine dissolution in alkaline solutions at -20, 4, and 22 °C from dissolution experiments that lasted up to 442 days. The range of temperatures chosen corresponds to those that can be achieved in mid- to large-sized icy worlds from radiogenic sources alone, in the absence of extra heat due to tidal friction[4,5,7]. Most icy worlds with diametres exceeding 400-500 km cross this temperature threshold when their cores, comprised of ice and rock, undergo an initial heating period. Three different solution chemistries were used at each temperature to analyse the effect of NH_3 concentration (0, 0.8, 8.0 mass % - hereafter %) and pH in an alkaline, dilute saline solution (H_2O-NaCl-KCl-$NaHCO_3$), such as is thought to evolve in

38 solutions interacting with a chondritic rock matrix[8,9] and corroborated by analyses of vapour
39 and grains emitted in Enceladus' plumes[2]. At -20 °C, some unfrozen solution existed in all
40 experiments as the NaCl-KCl-$NaHCO_3$-H_2O system has a eutectic temperature (solidus) of -
41 24 °C[10], while the H_2O-NH_3 system has a eutectic temperature of -96 °C[11] (Supplementary
42 Information 4.1-4.2 and Supplementary Fig. 5). The amount of solution that remains unfrozen
43 increases with increasing NH_3 content (Table 1). At experimental conditions pure water ice
44 formed during freezing[10,11].

45 Optical microscope images of partially frozen 0.0, 0.8 and 8.0% NH_3 solutions illustrate
46 decreasing crystallinity and increasing porosity in the ice phase caused by increasing NH_3
47 content (Fig. 1a-c). Visual evidence of an unfrozen solution film at the olivine-ice interface
48 was obtained by imaging melt propagation from the ice-olivine boundary in a frozen sample
49 allowed to equilibrate to bench temperature (Fig. 1d), and an in-situ investigation of olivine
50 grains in frozen solutions (Fig. 1e). To identify solutes concentrated in the unfrozen film at
51 the olivine interface, Raman analyses were performed at -20 °C on an amalgam of olivine
52 grains, ice, and unfrozen solutions using a temperature-controlled stage. Raman spectra,
53 which probed the transition from ice to interfacial liquid water, show that the shape of the
54 broad symmetric and asymmetric OH-stretching band of water at 2900–3800 cm^{-1} evolves
55 when approaching the olivine surface, characterized by an upward shift of the entire band and
56 a clear decrease in the intensity of the region <3325 cm^{-1} that corresponds to symmetric OH–
57 stretching (Supplementary Figs. 3, 4). In addition, the intensities of NH_3 and CO_3^{2-} peaks
58 positively correlate with the broadening and intensity decrease of the spectral component
59 centred at 3138 cm^{-1}, which is clearly defined in ice. These observations corroborate the
60 accumulation of NH_3 and CO_3^{2-} in the unfrozen solution enveloping the olivine grains.

61 Increasing silica and magnesium concentrations with time indicate that olivine dissolution
62 occurred continuously at all experimental conditions (Fig. 2a-c). We derived separate

apparent olivine dissolution rates (mol m^{-2} s^{-1}) from aqueous [Si] and [Mg] (denoted r_{Si} and r_{Mg}), and split them into two regimes based on reaction progress: initial rates (furthest from equilibrium, $\Delta G_{diss} << 0$; 0-14d) and long-term rates (closer to equilibrium, $\Delta G_{diss} < 0$; 167d). These rates are "apparent" as any sequestration of Mg or Si in secondary phases decreases their respective aqueous concentrations, resulting in lower calculated olivine dissolution rates.

The initial apparent dissolution rates r_{Si} and r_{Mg} are relatively clustered at -20 °C, indicating nearly stoichiometric alteration (Fig. 2d). With increasing temperature r_{Si} and r_{Mg} increasingly diverge from one another, with r_{Mg} generally lower than r_{Si}. The majority of the initial r_{Si} and r_{Mg} also show a modest increase with increasing temperature from -20 to 4 °C, whereas from 4 to 22 °C, two of the r_{Si} rates and all of the r_{Mg} show no meaningful dependence on temperature (Methods). Previous experimental studies that characterized olivine dissolution at below 0 °C focused on highly acidic solutions[14,15], and rapid dissolution rates were ascribed to an acid concentration effect in an unfrozen fluid phase[15]. However, as the mechanism of olivine dissolution is thought to change from acid to alkaline conditions[12], acid-pH olivine dissolution rates cannot be directly applied to alkaline conditions. The overall trends from our experiments show a weak inverse relation between pH and dissolution rates in the alkaline pH range, consistent with published alkaline olivine dissolution rates at ambient temperatures[12,13]. In contrast, the individual r_{Si} show a positive correlation with ammonia concentration at a given pH: despite having identical pH at 22 °C, r_{Si} is higher in all experiments with 0.8% NH_3 compared to 0% NH_3 (Fig. 2d).

Long-term apparent rates (ltr_{Si} and ltr_{Mg}) decrease with temperature from -22 to 4 °C but are roughly equivalent at 4 and 22 °C (Fig. 2e). All rates appear to approach steady state at 167d, while the experiments that lasted 442d (0.8% NH_3) show a curious increase in concentrations (Fig. 2a-c; 167-443d), correlating to a slight transient increase in rates. In terms of stoichiometry, $ltr_{Mg} > ltr_{Si}$ at -20 °C, but at 4 and 22 °C ltr_{Si} and ltr_{Mg} generally come close to

converging ($ltr_{Mg} \geq ltr_{Si}$). Long-term ltr_{Si} are relatively constant with increasing pH at 4 and 22 °C, with only a weak positive relation recorded at -20 °C.

All of the experiments displayed varying degrees of non-stoichiometric olivine alteration behaviour, with $r_{Si} > r_{Mg}$ or $ltr_{Mg} \geq ltr_{Si}$. The increasing degree of non-stoichiometry in r_{Si} and r_{Mg} with temperature, as well as very low activation energies, are evidence that released Mg and Si were being pulled out of solution and incorporated into secondary authigenic phases (Methods). Finally, the non-stoichiometric long-term rates at -20 °C indicate potential secondary phase formation occurring even in the partially frozen experiments (Fig. 2e). Both the initial (r_{Si}, r_{Mg}) and long-term (ltr_{Si}, ltr_{Mg}) apparent rates calculated at 4 and 22 °C cannot, therefore, be considered equivalent to far-from-equilibrium olivine dissolution rates (Supplementary Information 2.2). Our apparent rates rather describe an overall alteration process occurring at conditions much closer to equilibrium, and thus more similar to the rates expected on icy bodies.

Observation of olivine grains at the micron scale (SEM) revealed no visible alteration features at the olivine surface (Fig. 3a). However, at the nanoscale, evidence of the formation of a non-crystalline (amorphous) secondary phase at the olivine surface is apparent. In high-resolution iDPC-STEM images (Fig. 3b), the olivine lattice fringes abruptly terminate at a surface altered layer (SAL), here an irregular <1 nm-wide band of material without an ordered structure (Fig. 3b). The long-term dissolution rates ($ltr_{Mg} > ltr_{Si}$; Fig. 2e) suggest possible preferential sequestration of Si in this SAL. From the aqueous chemistry we further calculated the theoretical thicknesses of SALs (Supplementary Information 2.3); typical values were found to be <10 Å, consistent with our observations.

We propose that the mechanism for this alteration is the unfrozen film of solution at the ice-olivine interface, which may also be enriched in ammonia due to its exclusion from the ice

112 phase. During melting/refreezing, the chemical potential at the solution-mineral interface
113 causes an interfacial liquid film to form around mineral grains that persists below the partial
114 freezing point (liquidus) and even the total freezing point (solidus) of the bulk solution[16,17].
115 The olivine alteration observed in our experiments validates a proposed mechanism for
116 aqueous mineral alteration signatures previously observed in chondrites[18] and in extreme
117 environments in Antarctica[19]. Alteration at sub-zero temperatures at alkaline conditions has
118 far-reaching implications for interpreting the present day mineralogy of the rocky cores of icy
119 worlds, as exothermic mineral weathering is predicted at any temperature where this liquid
120 film forms, further enhanced by antifreeze agents (salts, NH_3) that increase the width of this
121 film and thus the liquid water-rock ratio[17].

122 Based on long-term rates observed at -20 °C in our experiments (Fig. 2e), we assessed that the
123 heating rate generated by olivine dissolution (up to 2.3×10^{-8} to 4.6×10^{-7} W kg^{-1}, Methods) is
124 comparable to that generated by short-lived radioactive nuclides (e.g., ^{26}Al) , and may provide
125 a heat pulse for periods of tens to hundreds of millions years after accretion[4,5]. We posit that
126 during progressive radiogenic heating of initially frozen interiors, aqueous alteration should
127 commence at least when the first aqueous melts appear in the deepest regions (as low as -96
128 °C, depending on volatile and salt contents). Melting is expected to propagate throughout the
129 entire core at timescales ranging between a few tens to hundreds of millions of years,
130 depending on the body size and available heat sources[4,5]. Given the relatively fast apparent
131 dissolution rates observed in our experiments, we predict that alteration will be controlled by
132 the outward propagation rate of melt front, resulting in alteration of most of the silicate core.
133 This process likely controlled the early evolution of most icy worlds, including Ceres,
134 Saturn's and Uranus' mid-sized moons (Mimas, Enceladus, Dione, Ariel, Oberon, Titania)[1],
135 and TNOs with diameters >500 km[7]. Low core densities of Ceres (2400-2900 kg m^{-3})[20],
136 Enceladus (2400-2500 kg m^{-3})[21], and Dione (2400-2500 kg m^{-3})[22] corroborate the hypothesis

that the rocky cores of these worlds are largely composed of altered hydrated minerals.

This initial period of geologically-rapid chemical alteration of primary ultramafic minerals (Fe and Mg-rich silicates, such as olivine, pyroxene), associated with H_2 production[23], may have produced potentially habitable rock-water-hosted environments even at relatively low temperatures. After this first widespread alteration stage, active alteration of primary minerals was likely limited to only a few bodies in the Solar system where fresh minerals are continuously brought in contact with water, notably on Earth at mid-oceanic ridges, but also possibly on Europa's seafloor[24].

Even though our data support a new scenario where serpentinization reactions no longer play a major role on icy moons, this does not imply that these bodies are geochemically quiescent. For instance, chemical data from Enceladus should now be viewed within the framework of water-rock interactions other than serpentinization of primary minerals: our results suggest that the low yields of H_2 may be explained by oxidization of Fe(II) in secondary minerals such as serpentine, siderite and Fe-bearing brucite[2]. Alternatively, other processes may be ongoing, such as hydrothermal pyrolysis of primordial organics or biotic methanogenesis, as recently invoked to explain the rough equivalence of H_2 and CH_4 in the plumes of Enceladus[25].

More generally, our results imply that secondary altered minerals should be ubiquitous in the interiors of icy moons and parent bodies of carbonaceous chondrites. Altered mineral assemblages in the samples retrieved by Hayabusa2 and OSIRIS-Rex, including detailed investigations of SALs, will provide crucial information about past aqueous environments in the parent bodies of Ryugu and Bennu[26]. Similar to what was observed on Ceres with Dawn[27], identification of alteration products by the upcoming observation campaigns using the James Webb Spatial Telescope and the Lucy mission to the Trojan asteroids may confirm the ubiquity of aqueous processes, even in distant icy worlds.

Methods

Batch reactor experiments were carried out at -20, 4 and 22 °C for variable periods of time ranging from 41 to 442 days. Three experimental series were carried out at each temperature, with each series being comprised of numerous Nalgene vials, each containing 0.3 g of San Carlos olivine grains ($Mg_{1.83}Fe_{0.17}SiO_4$) sieved to 0.05-0.125 mm size range, and 30 mL of saline fluid containing either 0.0, 0.8, or 8.0 mass % NH_3 (0.0 % NH_3 solution prepared with NaOH). The starting $pH_{(25\ °C)}$ values of the solutions were 10.8, 10.8, and 12.2, respectively. Vials were then sequentially removed from the experiment at designated times and sampled post-mortem (fluid chemistry shown in Fig. 2a-c). All experiments were carried out at ambient pressure (1 bar). Pressure is not a crucial variable as pressures in mid-sized icy bodies that maintain relevantly low temperatures will have correspondingly low pressures (for example, <400 bar maximum in a core the size of Enceladus'[28]), at which pressure is not known to have significant effects on olivine alteration processes[29]. Mg-rich olivine (forsterite) was selected for these experiments as a common and dominant primary mineral found in the chondrites[30,31] that are thought to make up icy worlds[2,3,9]. In addition, olivine is of specific interest as a primary mafic mineral that drives serpentinization reactions and the production of H_2[1,9]. The overall composition, ratios of salts, and NH_3 concentrations of the solution were chosen to bracket the chemistry of solutions predicted to evolve from chondrite-fluid interactions[32,33]. Additional information on the experimental approach is discussed in Supplementary Information 1.1-1.3.

The olivine dissolution reaction at our experimental conditions can be represented by:

$$Mg_{1.83}Fe_{0.17}SiO_4 + 4H^+ \rightarrow 1.83Mg^{2+} + 0.17Fe^{2+} + SiO_2(aq) + 2H_2O$$

This reaction is related but distinct from a serpentinization reaction. Based on the two olivine solid solution end members, serpentinization reactions can be expressed as follows:

186 $2Mg_2SiO_4$ (forsterite) + $3H_2O$ → $Mg_3Si_2O_5(OH)_4$ (serpentine) + $Mg(OH)_2$ (brucite)

187 $3Fe_2SiO_4$ (fayalite) + $2H_2O$ → $2Fe_3O_4$ (magnetite) + $3SiO_2$ + 2H

188 There is currently no consensus whether a lower temperature bound for serpentinization
189 exists. Studies postulate these reactions continue down to 10 °C[23], although recent field
190 studies of ophiolite weathering suggest that observed H_2 and CH_4 production at low
191 temperatures are attributable to later stages of water-rock interaction with secondary, rather
192 than primary, minerals[34]. While our experiments were limited in time (max. 442 days), we can
193 speculate that over significantly longer time periods the amorphous SALs that formed on the
194 olivine grains could serve as a matrix for the in situ nucleation of poorly crystalline proto-
195 serpentine phase(s), especially in light of the chemical oversaturation with respect to
196 serpentine minerals in many of our experiments (Supplementary Information 4.3 and 4.4).
197 Such proto-serpentines have been observed as a precursor step in serpentinization reactions[35].

198 The major aqueous cations were analysed by inductively coupled plasma atomic emission
199 spectroscopy (ICP-AES). Apparent dissolution rates were calculated from the aqueous
200 concentrations of Mg and Si: initial apparent dissolution rates (r_{Si} and r_{Mg}) were calculated
201 based on linear regressions of the concentration data from t = 0 to 14 d; long-term apparent
202 rates (ltr_{Si} and ltr_{Mg}) were derived from the dc/dt slope of the aqueous concentration data at
203 167d (Supplementary Information 2.1 and Supplementary Fig. 1). Rates based on aqueous Fe
204 concentrations were not calculated as this element was generally below analytical detection
205 limits (Supplementary Information 6). As a reminder concerning mineral dissolution kinetics,
206 the concentrations of Si and Mg at a given time in a reactor reflect the dynamic relation
207 between two fundamental processes: their release from the olivine structure and their
208 subsequent incorporation into secondary authigenic phases (both crystalline and amorphous-
209 see details in Supplementary Information 2.3). The degree of incorporation into authigenic
210 phases is both element-specific and depends on temperature and other physico-chemical

parameters. Because the formation of authigenic phases decreases the aqueous concentrations of the element(s) used to calculate the thermal activation energy E_a (Si, Mg), this decreases the slope of the ln k vs $1/T$ relation used to calculate E_a (Supplementary Fig. 2). The attenuated dependency of r_{Si} on temperature that we measured is therefore reflected in the thermal activation energies (E_a = 12-19 kJ mol^{-1}) determined from the initial apparent rates of olivine dissolution at T = -20, 4 and 22 °C. These values are lower than the average value of ~63 kJ mol^{-1} from compiled rate data[13]. Further details on the calculation of E_a are given in Supplementary Information 2.1-2.2; derived rates are listed in Supplementary Table 1.

The heating rate of olivine dissolution was calculated from the average ltr_{si} (1.2×10^{-13} mol m^{-2} s^{-1}) of all experiments at -20 °C (Fig. 2), with a ΔH of 203 kJ mol^{-1} released during dissolution[36]. Heating rates can then be scaled to surface areas to calculate heating rates for a mass unit of olivine having grain sizes different from those used in our experiments. The range of heating rates presented above were calculated using geometric surface areas for olivine grain sizes common to chondrites (0.05-1 mm radius, with surface areas of 18.5-0.923 m^2 kg^{-1})[31].

To image olivine in partially frozen aqueous solutions we used optical microscopy (plain and polarized light) to observe the nature of the olivine-ice interface and the porosity of the enveloping adjacent ice. The microscopy work was done in a cold room at -8 °C. The physical process of fluid melting at the olivine grain-ice interface was also studied with a mixture of unreacted olivine grains (crushed, sieved and cleaned identically to olivine used in the experiments, but not included in the experiments) and deionized water that was frozen with liquid N_2 (77 K). The frozen mixture was then observed under an optical microscope at ambient temperature so that we could record sequential images of the liquid solution front propagating away from the olivine grain as the temperature gradually rose. Raman analyses of olivine, ice, and unfrozen fluid were performed at the olivine-ice interface using a Renishaw®

InVia confocal Raman microscope. Samples (unreacted olivine grains and solution) were placed in a quartz cell in a Linkam® THMS 600 heating/freezing stage and maintained at -20 °C during analyses. Measurements were performed at 532 nm using a 50x-long working distance objective.

Post-reaction olivine grains were imaged by field emission scanning electron microscopy (FEG SEM, Zeiss Ultra 55, CMTC, Univ. Grenoble Alpes) at 20 kV to characterize the presence and degree of surface coverage of potential secondary phases (crystalline and/or amorphous). Reacted olivine grains (10-15 grains total) originating from experiments in each solution were used for EDX spot analyses. For all analyses, conchoidal fracture surfaces were carefully selected to avoid any pre-existing alteration features on unaltered grains (Supplementary Information 5.1). SEM images and EDX analyses of grain surfaces from all grain sets did not reveal any dissolution features, such as etch pits, or surface precipitates. EDX spot analyses of post reaction surfaces were not distinguishable from those measured on unreacted olivine (in both cases, the nominal compositional stoichiometry of San Carlos olivine was confirmed). Some remaining surface fines (micrometre-sized grain fragments created during comminution) seem to have been present on both unreacted and reacted grains (e.g., Fig. 3a).

Detailed high-resolution analyses by transmission electron microscopy (TEM) were centred on three altered olivine grains subjected to 442 d of reaction at -20 °C in a 0.8 % NH_3 saline solution, as this experiment was subject to the longest reaction times. Here, the purpose was to examine structural and chemical changes to the near surface region, which included the formation of secondary phases, in the form of mineral (crystalline) phases or amorphous phases. We examined these samples in cross section with electron transparent foils prepared by focused ion beam (FIB) milling (Supplemental Information 5.2) using standard preparation techniques[37]. These observations were then compared to samples from unreacted olivine

grains prepared in an identical manner (Supplementary Figs. 6-9). TEM analyses were performed using a state-of-the-art Thermo Fisher Scientific Themis Z 3.1 operated at 300 kV, and a Tecnai F20 operated at 200 kV, both housed at the GFZ-PISA facility, Potsdam. We used standard bright and dark field (BF, DF), scanning TEM-high angle annular dark field (STEM-HAADF), and integrated Differential Phase Contrast STEM (iDPC-STEM) imaging techniques[38,39], while high resolution chemical analyses were carried out with EELS spectral imaging in STEM mode (Supplemental Information 5.3). The chemical composition of the very thin amorphous SALs (Fig. 3b) could not be measured because of their sensitivity to the electron beam. It is interesting to note that the extreme thinness of the SALs indicates that they would not have acted as a diffusion barrier to the release of Si and Mg from the olivine structure. On the other hand, diffusion limitations can potentially occur for much thicker (up to tens of nm) SALs[40].

Further details concerning methods, materials, instrumental parameters and techniques can be found in the Supplementary Information.

Data availability: Additional data and complete analysed fluid chemistries are included in Supplementary Information and Supplementary Tables 2-11.

Corresponding author: correspondence to A. Zandanel.

Acknowledgments: This study acknowledges the financial support from the French Agence Nationale de Recherche, project ANR OASIS (grant N° ANR-16-CE31-0023-01). We thank Y. Marrocchi for the raw San Carlos olivine and Selfrag AG (Kerzers, Switzerland) for the high voltage pulsed power fragmentation of the original San Carlos olivine sample. The use of equipment in the “Potsdam Imaging and Spectral Analysis Facility” (PISA) is acknowledged. The authors especially thank the European Regional Development Fund and the State of Brandenburg for the Themis Z TEM (part of PISA). Chemical analyses by ICP-AES and BET

surface area measurements were performed at the geochemistry-mineralogy platform of ISTerre (UGA, Grenoble, France), partially funded by a grant from Labex OSUG@2020. We also thank A. Schreiber (GFZ) for her help in developing the FIB technique used, N. Findling (ISTerre) for assistance with the sub-zero alteration experiments.

Author contributions: L.T. designed the project. A.Z. performed the experiments, ICP-AES analyses, and geochemical modelling. R.H. evaluated the kinetic behaviour of olivine dissolution and interpreted TEM results with V.R. FIB and TEM work was carried out by V.R. Raman analyses were performed and interpreted by M.M. The manuscript was written by A.Z., R.H., G.T., and L.T., with contributions from all co-authors. All co-authors contributed to the discussion and interpretation of the data.

Competing interests: The authors declare no competing interests.

Tables

Table 1

Table 1: Physiochemical parameters									
Solution	NaOH (0 % NH_3)			0.8 mass % NH_3			8.0 mass % NH_3		
Temp (°C)	22	4	-20	22	4	-20	22	4	-20
Fluid : Ice	30 : 0	30 : 0	1 : 29	30 : 0	30 : 0	2 : 28	30 : 0	30 : 0	13 : 17
Fluid : Rock	100 : 1	100 : 1	2 : 1	100 : 1	100 : 1	6 : 1	100 : 1	100 : 1	42 : 1
Ionic strength	0.1	0.1	5.1	0.11	0.11	1.89	0.09	0.09	0.22
Molal NH_3	0	0	0	0.5	0.5	6.7	4.7	4.7	9.6
In-situ pH	10.8	11.1	11.5	10.8	11.5	11.9	12.1	12.8	13.7
Duration (days)	167	167	41	442	442	442	41	167	167

Table 1: Initial physiochemical characteristics of each experiment.

"Fluid : Ice" indicates the mass ratio of unfrozen solution remaining to the moles of ice formed in each reactor. "Fluid : rock" indicates the mass ratio of unfrozen solution in each reactor to olivine, not including the mass of the unfrozen solution films at the mineral grain surface. Ionic strength, molal NH_3, and in-situ pH refer to properties of the in-situ unfrozen solution. In-situ pH was calculated with the code FREZCHEM[10] from the measured bench temperature of each solution, and increases due to temperature effects at 4 °C, and due to temperature effect and solute exclusion from the ice phase at -20 °C. Note that at 22 °C the pH of the 0.8 % NH_3 solution is identical to the 0 % solution, but is lower than that of the 0 % solution at 4 °C and -20 °C.

Display elements legends (Figures submitted separately)

Fig. 1: Characterization of the ice, unfrozen solution, and ice-olivine interface.

a-c: Images taken by an optical microscope in polarized transmission mode of the three solutions used in this study at -8°C: **a.** 0.0 % NH_3. **b.** 0.8 % NH_3. **c.** 8.0 % NH_3. Increased birefringence (highest birefringence visible as vivid blue) of the ice phase indicates increased crystallinity (Supplementary Information 3.1). Crystallinity of the ice phase increases with decreasing NH_3 content. **d.** Image of olivine crystals and deionized water flash-frozen with liquid N_2 and rapidly imaged under a microscope at room temperature to capture outward propagation of melt. **e.** Representative image of olivine in frozen solution taken with non-polarized light. **f.** Annotated compilation of three Raman spectra collected at -20 °C with spectral resolution 0.3-1 cm^{-1}. Two insets show the peaks unique to the spectra collected at the ice-olivine boundary. The gradual phase transitions recorded in the interfacial region are an instrumental artifact, the true gradients are much sharper (Supplementary Information 3.2).

Fig. 2: Measured [Si] and [Mg] concentrations over time and calculated olivine dissolution rates over temperature.

a. b. c. Concentrations of Si (circles) and Mg (diamonds) (mmol $L^{-1} \times 10^{-2}$) in the fluid for the longest running experiment sets (0.8 % NH_3) at each experimental temperature. Concentrations at -20 °C (**c**) are for the bulk (melted) solution. Error bars indicate instrumental error. **d.** Initial (0-14 day) apparent dissolution rates r_{Si} and r_{Mg} over temperature. Divergence between values for r_{Si} and r_{Mg} in the same experiment indicates that the rates become more non-stoichiometric with increasing temperature. **e.** Long-term (167 day) dissolution rates ltr_{Si} and ltr_{Mg} with respect to temperature for all experiments (two experiments were excluded due to reactor failure: see Supplementary Information 6). Error bars show error calculated from summing standard errors of each sample used in the rate analysis and standard deviations of the replicate samples at 167 h. In all panels, where error bars are not visible, error is smaller than the symbols.

Fig. 3: Solid-state analysis of an olivine grain reacted in 0.8 mass % NH_3 for 442 days at -20 °C.

a. SEM image of reacted olivine sample surface showing location where the FIB foil was cut (arrow). Note the lack of any obvious surface precipitates or etch pits. **b.** FIB-prepared TEM foil of the same altered sample imaged by iDPC-STEM. The interfacial region is characterized by lattice fringes of unaltered olivine and an Au layer applied before FIB preparation (post-reaction surface). The two phases are separated by a thin surface altered layer (SAL) lacking an ordered structure. The SAL delimits the position of the solvent-olivine interface when the grain was removed from solution. The colored atoms represent an atomic-scale overlay of the forsterite olivine structure.

References

1. Vance, S. D. & Melwani Daswani, M. Serpentinite and the search for life beyond Earth. *Philos. Trans. R. Soc. A* **378**, (2020).
2. Waite, J. *et al.* Cassini finds molecular hydrogen in the Enceladus plume: Evidence for hydrothermal processes. *Science* **356**, 155–159 (2017).
3. Hsu, H.-W. *et al.* Ongoing hydrothermal activities within Enceladus. *Nature* **519**, 207–210 (2015).
4. Malamud, U. & Prialnik, D. Modeling Kuiper belt objects Charon, Orcus and Salacia by means of a new equation of state for porous icy bodies. *Icarus* **246**, 21–36 (2015).
5. Malamud, U. & Prialnik, D. A 1-D evolutionary model for icy satellites, applied to Enceladus. *Icarus* **268**, 1–11 (2016).
6. Palguta, J., Schubert, G. & Travis, B. J. Fluid flow and chemical alteration in carbonaceous chondrite parent bodies. *Earth Planet. Sci. Lett.* **296**, 235–243 (2010).

7. Guilbert-Lepoutre, A., Prialnik, D. & Métayer, R. Internal structure and cryovolcanism on Trans-Neptunian objects. in *The Trans-Neptunian Solar System* 183–201 (Elsevier, 2020).
8. Ohnishi, I. & Tomeoka, K. Hydrothermal alteration experiments of enstatite: implications for aqueous alteration of carbonaceous chondrites. *Meteorit. Planet. Sci.* **42**, 49–61 (2007).
9. Sekine, Y. *et al.* High-temperature water–rock interactions and hydrothermal environments in the chondrite-like core of Enceladus. *Nat. Commun.* **6**, 8604 (2015).
10. Marion, G. M. & Kargel, J. S. *Cold aqueous planetary geochemistry with FREZCHEM: from modeling to the search for life at the limits*. (Springer Science & Business Media, 2007).
11. Marion, G., Kargel, J., Catling, D. & Lunine, J. Modeling ammonia–ammonium aqueous chemistries in the Solar System's icy bodies. *Icarus* **220**, 932–946 (2012).
12. Pokrovsky, O. S. & Schott, J. Kinetics and mechanism of forsterite dissolution at 25 °C and pH from 1 to 12. *Geochim. Cosmochim. Acta* **64**, 3313–3325 (2000).
13. Rimstidt, J. D., Brantley, S. L. & Olsen, A. A. Systematic review of forsterite dissolution rate data. *Geochim. Cosmochim. Acta* **99**, 159–178 (2012).
14. Hausrath, E. & Brantley, S. L. Basalt and olivine dissolution under cold, salty, and acidic conditions: What can we learn about recent aqueous weathering on Mars? *J. Geophys. Res. Planets* **115**, E12001 (2010).
15. Niles, P. B., Michalski, J., Ming, D. W. & Golden, D. Elevated olivine weathering rates and sulfate formation at cryogenic temperatures on Mars. *Nat. Commun.* **8**, 998 (2017).
16. Anderson, D. M. The interface between ice and silicate surfaces. *J. Colloid Interface Sci.* **25**, 174–191 (1967).
17. Barer, S., Churaev, N., Derjaguin, B., Kiseleva, O. & Sobolev, V. Viscosity of nonfreezing thin interlayers between the surfaces of ice and quartz. *J. Colloid Interface Sci.* **74**, 173–180 (1980).
18. Rietmeijer, F. J. A model for diagenesis in proto-planetary bodies. *Nature* **313**, 293–294 (1985).
19. Dickinson, W. W. & Rosen, M. R. Antarctic permafrost: An analogue for water and diagenetic minerals on Mars. *Geology* **31**, 199–202 (2003).
20. Park, R. *et al.* A partially differentiated interior for (1) Ceres deduced from its gravity field and shape. *Nature* **537**, 515–517 (2016).

21. Iess, L. *et al.* The gravity field and interior structure of Enceladus. *Science* **344**, 78–80 (2014).
22. Zannoni, M., Hemingway, D., Casajus, L. G. & Tortora, P. The gravity field and interior structure of Dione. *Icarus* **345**, 113713 (2020).
23. Bach, W. Some compositional and kinetic controls on the bioenergetic landscapes in oceanic basement. *Front. Microbiol.* **7**, 107 (2016).
24. Běhounková, M. *et al.* Tidally Induced Magmatic Pulses on the Oceanic Floor of Jupiter's Moon Europa. *Geophys. Res. Lett.* **48**, e2020GL090077 (2021).
25. Affholder, A., Guyot, F., Sauterey, B., Ferrière, R. & Mazevet, S. Bayesian analysis of Enceladus's plume data to assess methanogenesis. *Nat. Astron.* 1–10 (2021).
26. Brunetto, R. & Lantz, C. Laboratory perspectives on sample returns from Hayabusa2 and OSIRIS-REx. *Nat. Astron.* **3**, 290–292 (2019).
27. Marchi, S. *et al.* An aqueously altered carbon-rich Ceres. *Nat. Astron.* **3**, 140–145 (2019).
28. Choblet, G. *et al.* Powering prolonged hydrothermal activity inside Enceladus. *Nat. Astron.* **1**, 841 (2017).
29. O'Hanley, D. S. *Serpentinites: records of tectonic and petrological history*. (Oxford University Press on Demand, 1996).
30. Rubin, A. E., Trigo-Rodríguez, J. M., Huber, H. & Wasson, J. T. Progressive aqueous alteration of CM carbonaceous chondrites. *Geochim. Cosmochim. Acta* **71**, 2361–2382 (2007).
31. Rubin, A. E. Size- frequency distributions of chondrules in CO3 chondrites. *Meteoritics* **24**, 179–189 (1989).
32. Zolotov, M. Y. An oceanic composition on early and today's Enceladus. *Geophys. Res. Lett.* **34**, L23203 (2007).
33. Glein, C. R., Baross, J. A. & Waite, J. The pH of Enceladus' ocean. *Geochim. Cosmochim. Acta* **162**, 202–219 (2015).
34. Miller, H. M. *et al.* Modern water/rock reactions in Oman hyperalkaline peridotite aquifers and implications for microbial habitability. *Geochim. Cosmochim. Acta* **179**, 217–241 (2016).

35. Lafay, R., Fernandez-Martinez, A., Montes-Hernandez, G., Auzende, A. L. & Poulain, A. Dissolution-reprecipitation and self-assembly of serpentine nanoparticles preceding chrysotile formation: Insights into the structure of proto-serpentine. *Am. Mineral.* **101**, 2666–2676 (2016).
36. Ball, J. & Nordstrom, D. *User's Manual for WATEQ4F, with Revised Thermodynamic Data Base and Test Cases for Calculating Speciation of Major, Trace, and Redox Elements in Natural Waters.* 189 (1991).
37. Schaffer, M., Schaffer, B. & Ramasse, Q. Sample preparation for atomic-resolution STEM at low voltages by FIB. *Ultramicroscopy* **114**, 62–71 (2012).
38. Lazić, I., Bosch, E. G. & Lazar, S. Phase contrast STEM for thin samples: Integrated differential phase contrast. *Ultramicroscopy* **160**, 265–280 (2016).
39. Bosch, E. G. & Lazić, I. Analysis of HR-STEM theory for thin specimen. *Ultramicroscopy* **156**, 59–72 (2015).
40. Daval, D. *et al.* Influence of amorphous silica layer formation on the dissolution rate of olivine at 90 °C and elevated pCO_2. *Chem. Geol.* **284**, 193–209 (2011).

431

432

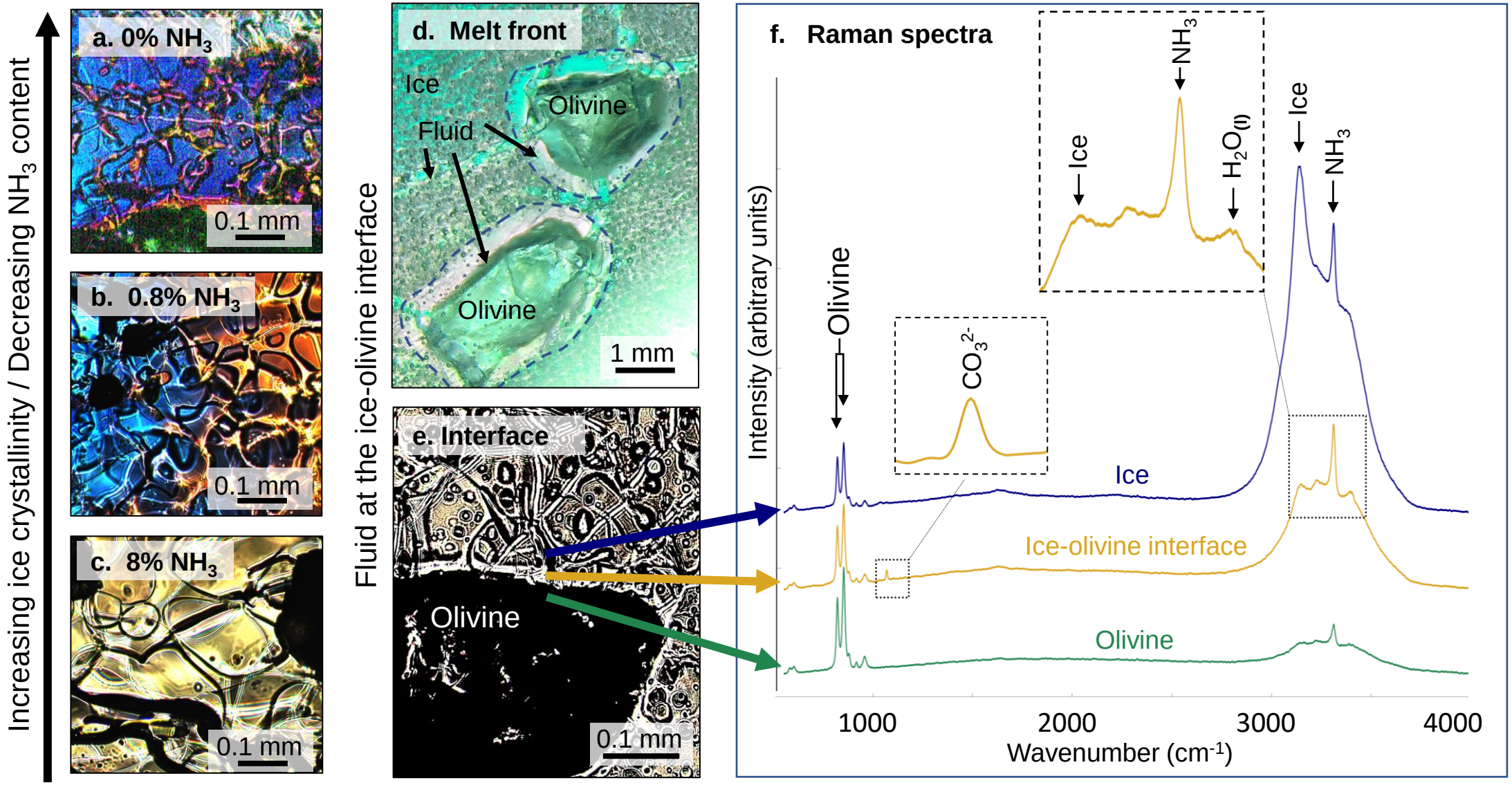
Increasing ice crystallinity / Decreasing NH_3 content
a. 0% NH_3
0.1 mm
b. 0.8% NH_3
0.1 mm
c. 8% NH_3
0.1 mm
Fluid at the ice-olivine interface
d. Melt front
Ice
Fluid
Olivine
Olivine
1 mm
e. Interface
Olivine
0.1 mm
f. Raman spectra
Intensity (arbitrary units)
Olivine
CO_3^{2-}
Ice
NH_3
$H_2O_{(l)}$
Ice
NH_3
Ice
Ice-olivine interface
Olivine
1000
2000
3000
4000
Wavenumber (cm^{-1})

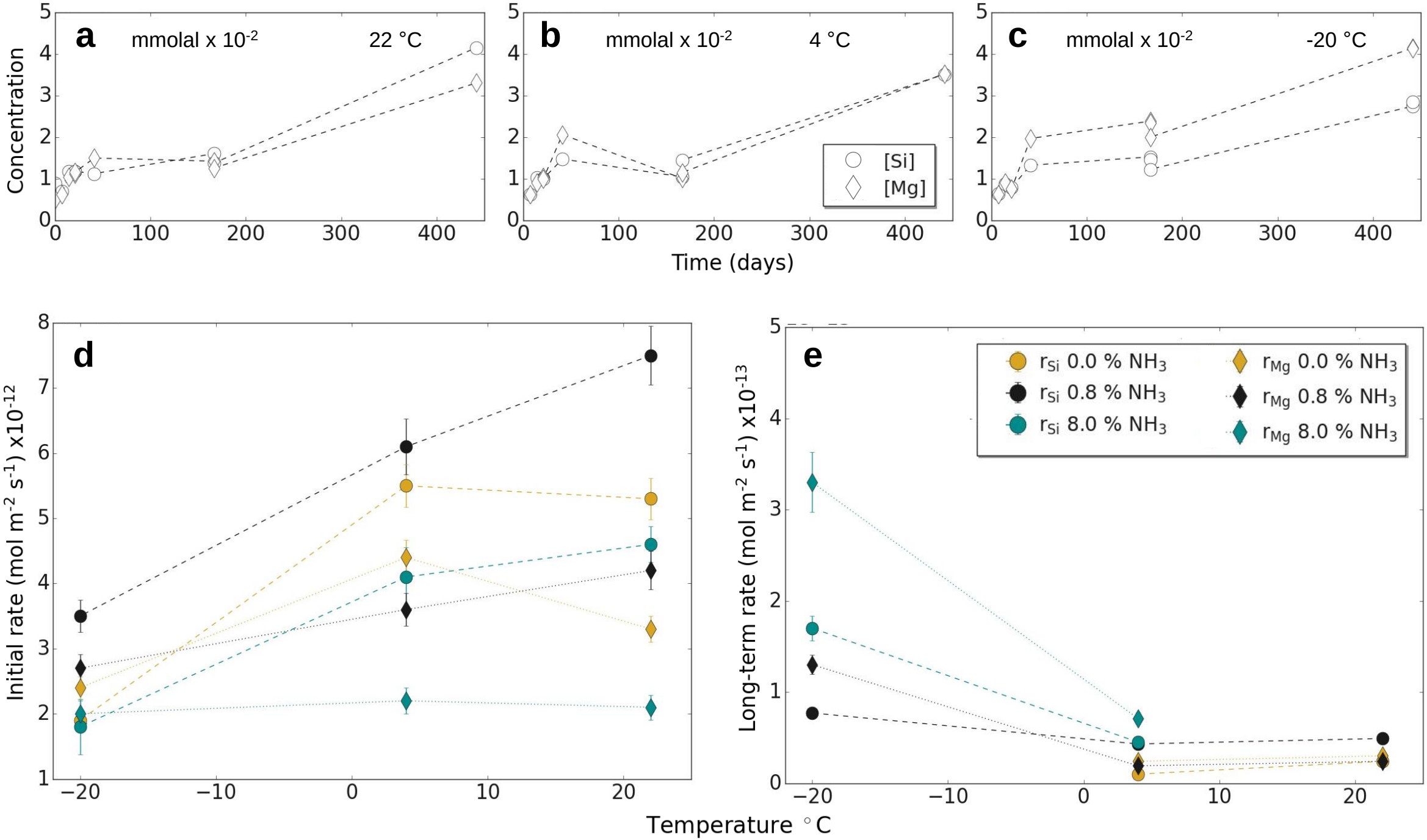
a
mmolal x 10-2
22 °C
b
mmolal x 10-2
4 °C
c
mmolal x 10-2
-20 °C
Concentration
Time (days)
[Si]
[Mg]
d
Initial rate (mol m-2 s-1) x10-12
e
Long-term rate (mol m-2 s-1) x10-13
rSi 0.0 % NH3
rSi 0.8 % NH3
rSi 8.0 % NH3
rMg 0.0 % NH3
rMg 0.8 % NH3
rMg 8.0 % NH3
Temperature °C

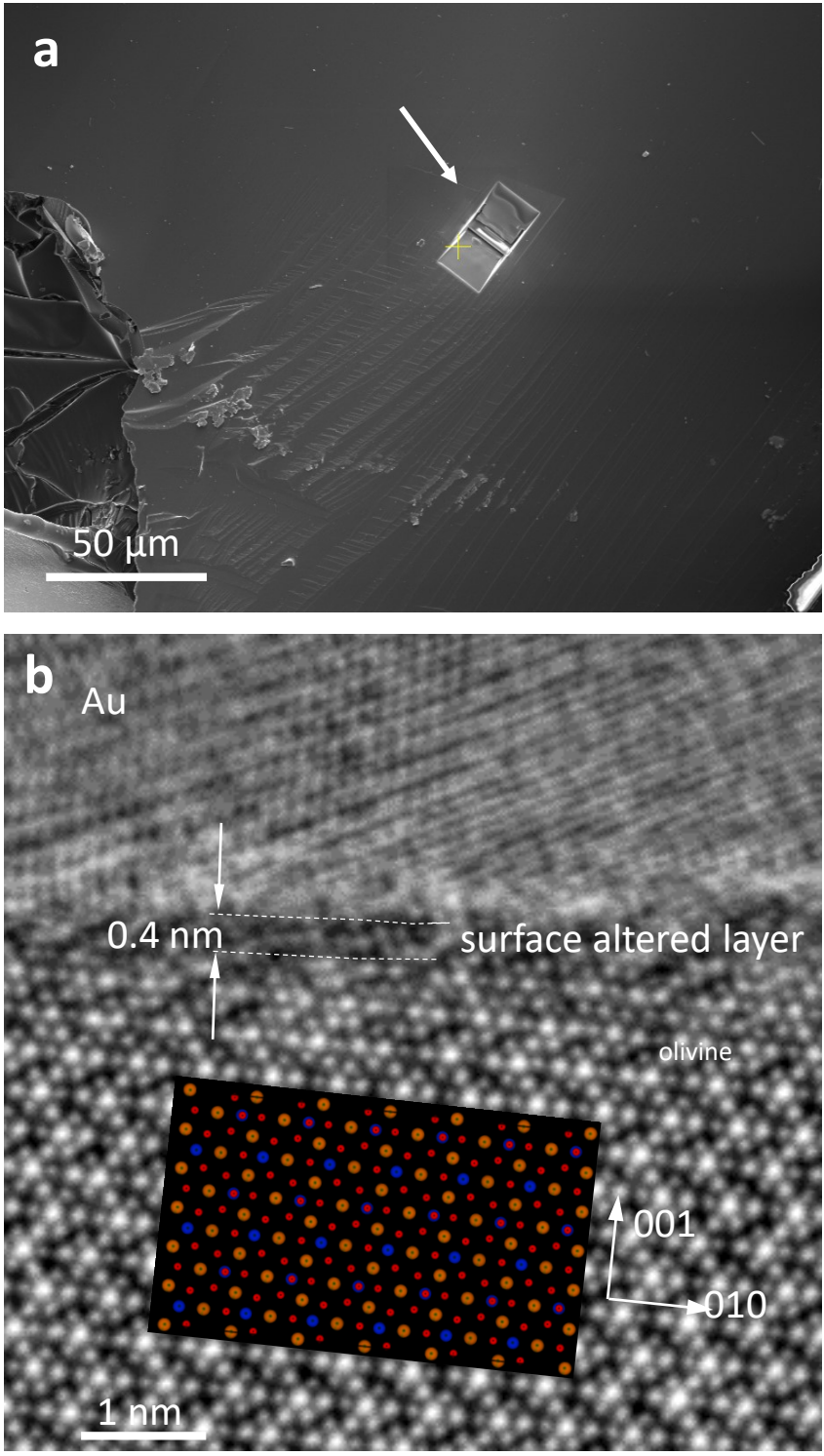
a
50 µm
b
Au
0.4 nm
surface altered layer
olivine
001
010
1 nm
Si
O
Fe/Mg